Phase coexistence near the polymorphic phase boundary

Oscar A. Torres Matheus[a], R. Edwin García[b], Catherine M. Bishop[a,*]

[a]*Department of Mechanical Engineering, University of Canterbury, Private Bag 4800, Christchurch, 8140 New Zealand*
[b]*School of Materials Engineering, Purdue University, West Lafayette, IN 47907, USA*

Abstract

A novel multiphase field theory for ferroelectric systems in the vicinity of a polymorphic phase boundary (PPB) is developed by coupling the Landau-Devonshire thermodynamic potentials of the individual phases. The model naturally predicts metastable coexistence of the rhombohedral (R) and tetragonal (T) phases near the PPB temperature, $T_{PPB} = 43\,^{\circ}\mathrm{C}$, for the BZT-40BCT system, and provides a maximum temperature of coexistence, $T_{C,0} = 49.9\,^{\circ}\mathrm{C}$, in agreement with experiments. For $T > T_{PPB}$, results show that metastable coexistence of two ferroelectric phases is a result of a phase transformation-induced polarization rotation plus switching mechanism. Metastable domains of the low-temperature R phase coexist with the high-temperature, thermodynamically stable T phase for long periods of time, from minutes to hours. For $T < T_{PPB}$, the coexistence time is on the order of tens of seconds due to a decreased thermal energy that suppresses the polarization rotation plus switching mechanism. Further, the kinetics of macroscopic T→R phase transformation is accelerated by a large thermodynamic driving force and high mobility.

Keywords: Ferroelectric, interferroelectric transitions, phase field model, phase coexistence, phase stability

2010 MSC: 00-01, 99-00

*Corresponding author
Email address: catherine.bishop@canterbury.ac.nz (Catherine M. Bishop)

1. Introduction

Ferroelectric (FE) materials span a wide range of applications, including high-dielectric-constant capacitors [1]; electromechanical devices, such as sensors, actuators, transducers, micropositioning systems, piezoelectric fuel injectors and printing machines [2]; and, more recently, non-volatile memories [1]. In particular, $Pb(Zr,Ti)O_3$ or PZT has been the most widely used piezoelectric material due to its wide range of composition-dependent properties [3] and high electromechanical performance near its Morphotropic Phase Boundary (MPB) [1–3]. However, recent environmental restrictions on the use of lead have resulted in the identification of alternate chemistries, with equal or higher response [2, 4, 5].

The search for new lead-free materials depends on understanding the origin of electromechanical performance in the vicinity of the transition temperature where two different FE phases coexist [3], commonly termed the interferroelectric phase transition temperature to differentiate it from the paraelectric-ferroelectric transition temperature [4]. The phase transformation regimes are traditionally summarized in composition-temperature maps, or phase diagrams (*e.g.,* Figure 1). A phase boundary representing a compositionally driven interferroelectric transition is referred to as an MPB [4, 5]. A phase boundary representing an interferroelectric transition driven by changes in temperature is referred to as a Polymorphic Phase Boundary (PPB) [4, 5]. Because the focus is on understanding the effect of temperature on material behaviour, the remainder of this paper will describe the equilibrium and phase transition kinetics in the vicinity of a PPB.

One promising lead-free candidate is $(1-x)Ba(Zr_{0.2}Ti_{0.8})O_3$-$x(Ba_{0.7}Ca_{0.3})TiO_3$ or $(1-x)$BZT-xBCT, which exhibits a PPB between the tetragonal (T) and rhombohedral (R) phases [6], Figure 1. Recently, the existence of an additional orthorhombic (O) phase has been speculated via high-resolution XRD and Rietveld refinement [7], Raman spectroscopy [8], and elastic, dielectric and piezoelectric measurements [9]. Gao *et al.* [5] have argued that the presence of the orthorhombic phase is inconclusive due to the narrow region of phase space in which the purported O phase appears, and the negligible difference in lattice parameter of the surrounding rhombohedral and tetragonal phases. Moreover, a region of R+T phase coexistence has been reported by experiments based on temperature-dependent dielectric permittivity and XRD measurements [10], micro-Raman scattering [11], CBED [12], and high-resolution XRD and Rietveld analysis [13].

The identification of three FE phases, R, O and T, would imply the existence of two

PPBs in the system as opposed to one, see Figure 1. Nevertheless, the presence of any one PPB is the origin of enhanced material properties [5], commonly associated with free energy flattening and low polarization anisotropy [14–16]. The latter results in minimal domain wall energy that causes miniaturization of the domain structure near the interferroelectric phase boundaries [17], and facilitates polarization rotation/extension [18]. It should be noted that, even though beyond the scope of this work, the classic Gibbs phase rule is violated for R+O+T+C coexistence, as indicated on Figure 1 at the intersection of the two PPBs as proposed by Keeble [7].

Theoretical work on ferroelectrics includes first-principles [19–24], atomic-level [25–30], and phase field modelling and simulations [14–16, 31–44]. First-principles approaches are typically based on the density functional theory [19], and have been successfully used to determine intrinsic material properties [19, 20], as well as to study domain walls [21] and domain patterns in nanowires [22], ultrathin films [23] and single-crystals [24]. Shell model molecular dynamics have been used to investigate domain nucleation and switching dynamics in single-crystals [25], size and strain effects on electric field-induced domain evolution in ultrathin films [28], and surfaces and domain wall energetics [29]. Further, molecular dynamics simulations based on effective Hamiltonians have been employed to investigate the mechanisms of polarization switching [27]. Nanoscale domain configurations and their evolution have also been studied by combining the shell model and the atomic-scale finite element method to improve computational performance [30].

Phase field formulations are traditionally built upon the Landau-Devonshire thermodynamic potential to describe the paraelectric-ferroelectric phase transition, and a polarization gradient energy penalty to account for domain walls [31]. Phase field descriptions have been extensively used for single-phase ferroelectrics to investigate microstructural evolution and domain configurations in single-crystals [32–37], polycrystals [38, 39], as well as in thin films [40, 41]. For the region near the interferroelectric phase boundary, phenomenological approaches commonly split the Landau coefficients into isotropic and anisotropic contributions to facilitate the thermodynamic analysis [14–16]. Structure symmetry is determined by identifying the easy polarization directions [15]. Landau coefficients are commonly fitted to experimental data of specific FE phases, and the accuracy of predicted properties is limited near interferroelectric transitions and bulk phases, *e.g.,* [45–47].

In spite of the great progress, the thermodynamic state and the material properties in the vicinity of the interferroelectric phase boundary remain under considerable debate [14]. Existing approaches cannot assess directly the impact of the transformation dynamics of multiple coexisting FE phases. This limitation can be overcome by considering the homogeneous free energy density of multiple coexisting FE phases separately [48], each with independent Landau coefficients obtained from experimental data for the respective phase. In this paper a new theory based on a multiphase field formulation is proposed to consider the thermodynamics of the two neighbouring phases. The model is applied to the BZT-40BCT system to demonstrate the mechanisms controlling the stabilization of the apparent O phase in the vicinity of the T-R phase boundary and elucidate the driving forces that determine their long term dynamics.

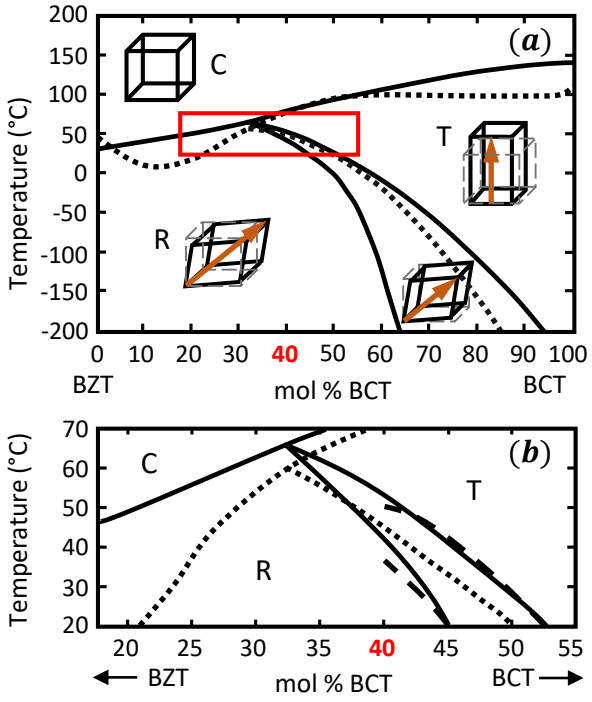

Figure 1: (a) BZT-xBCT pseudo-binary phase diagram, and (b) region of interest. Dotted lines correspond to single PPB between R and T phases, as reported by Liu and Ren [6]. Continuous lines indicate a purported O phase between the R and T phases (or the region of R+T coexistence), as reported by Keeble *et al.* [7]. Dashed lines are detailed phase boundaries depicted in region of interest, according to Ehmke [49].

2. Theoretical framework

We define the total Helmholtz free energy of a strain-free, two-phase FE system, where a polymorphic phase transition occurs at $T = T_{PPB}$ for a specific composition, as

$$F[\vec{P}, \phi; \vec{E}, T] = \int_V \left\{ f(\vec{P}, \phi; \vec{E}, T) + \frac{1}{2} \sum_{k,l=1}^{3} \sum_{i,j=1}^{3} K_{ijkl} \frac{\partial P_k}{\partial x_i} \frac{\partial P_l}{\partial x_j} + \frac{1}{2} \sum_{i,j=1}^{3} K_{ij} \frac{\partial \phi}{\partial x_i} \frac{\partial \phi}{\partial x_j} \right\} dV \tag{1}$$

where T is the temperature of interest, $\vec{P}$ is the polarization, $\vec{E}$ is the electric field, and ϕ is a phase field variable that specifies the region in space where each FE phase is locally stable. We set $\phi = 0$ as the low-temperature phase and $\phi = 1$ as the high-temperature phase. The first term on the right side of Equation 1 is the volumetric free energy density of the FE system, a continuous function of the controlling variables at the temperature of interest. The second term is the gradient energy penalty to create a domain wall (a polarization domain interface). K_{ijkl} is the $ijkl$-th gradient energy coefficient contribution for a polarization domain wall. The third term is the phase gradient energy penalty to create an interface between two phases. K_{ij} is the ij-th gradient energy coefficient contribution for a phase boundary .

The volumetric free energy density of the system is defined as

$$f(\vec{P}, \phi; \vec{E}, T) = f_0(\vec{P}; \vec{E}, T)[1 - h(\phi)] + f_1(\vec{P}; \vec{E}, T)h(\phi) + Wg(\phi) \tag{2}$$

where $h(\phi) = \phi^3(6\phi^2 - 15\phi + 10)$ is an interpolation function between the free energy densities of the two phases, f_0 and f_1; and $g(\phi) = \phi^2(1 - \phi)^2$ is a double-well potential that prevents unphysical phase transitions, see *e.g.,* [50].

For each phase, the volumetric free energy density is described by the Helmholtz thermodynamic potential, A, (a Landau-Devonshire potential) with respect to the cubic paraelectric phase, *i.e.,* [51]

$$A(\vec{P}; \vec{E}, T) = A(\vec{0}; \vec{0}, T) + \frac{1}{2}\alpha_i P_i^2 + \frac{1}{4}\alpha_{ij} P_i^2 P_j^2 + \frac{1}{6}\alpha_{ijk} P_i^2 P_j^2 P_k^2 - P_i E_i \tag{3}$$

where P_i is the ith polarization component (with $i, j, k = 1, 2, 3$), and α_i, α_{ij}, and α_{ijk} are the Landau coefficients. The leading coefficient is $\alpha_i = a_{CW}(T - T_{CW})$, where T_{CW} is the Curie-Weiss temperature and $a_{CW} > 0$ [51].

The free energy density is defined herein as $f(\vec{P};\vec{E},T) = A(\vec{P};\vec{E},T) - A(\vec{0};\vec{0},T_{CW,1})$, where $A(\vec{0};\vec{0},T_{CW,1})$ is the Helmholtz free energy of the reference state. Thus,

$$f_1(\vec{P};\vec{E},T) = \frac{1}{2}\alpha_{i,1}(T)P_i^2 + \frac{1}{4}\alpha_{ij,1}P_i^2P_j^2 + \frac{1}{6}\alpha_{ijk,1}P_i^2P_j^2P_k^2 - P_iE_i \tag{4}$$

$$f_0(\vec{P};\vec{E},T) = \frac{1}{2}\alpha_{i,0}(T)P_i^2 + \frac{1}{4}\alpha_{ij,0}P_i^2P_j^2 + \frac{1}{6}\alpha_{ijk,0}P_i^2P_j^2P_k^2 - P_iE_i + \Delta f_{PPB} \tag{5}$$

For a first order interferroelectric phase transition [14], $\Delta f_{PPB} = A_1(\vec{P}_{s1};\vec{0},T_{PPB}) - A_0(\vec{P}_{s0};\vec{0},T_{PPB})$, where $\vec{P}_{s1}$ is the spontaneous polarization of the high-temperature phase and $\vec{P}_{s0}$ is the spontaneous polarization of the low-temperature phase.

The proposed model is reference frame invariant and can be readily extended to describe polycrystalline systems, see *e.g.,* [39]. The model can also be adapted to include strain effects, see *e.g.,* [40]; and charged defects, see *e.g.,* [52].

Overall, the formulation naturally captures the structural R↔T phase transformation energetics, polarization energetics, and polarization-structural phase transformation interactions. Further, the coexistence and stability of phases near the PPB depend on the order of the two paraelectric-ferroelectric (P-FE) transitions, independently described by the free energy density of the individual FE phases with their own Landau coefficients, Figure 2.

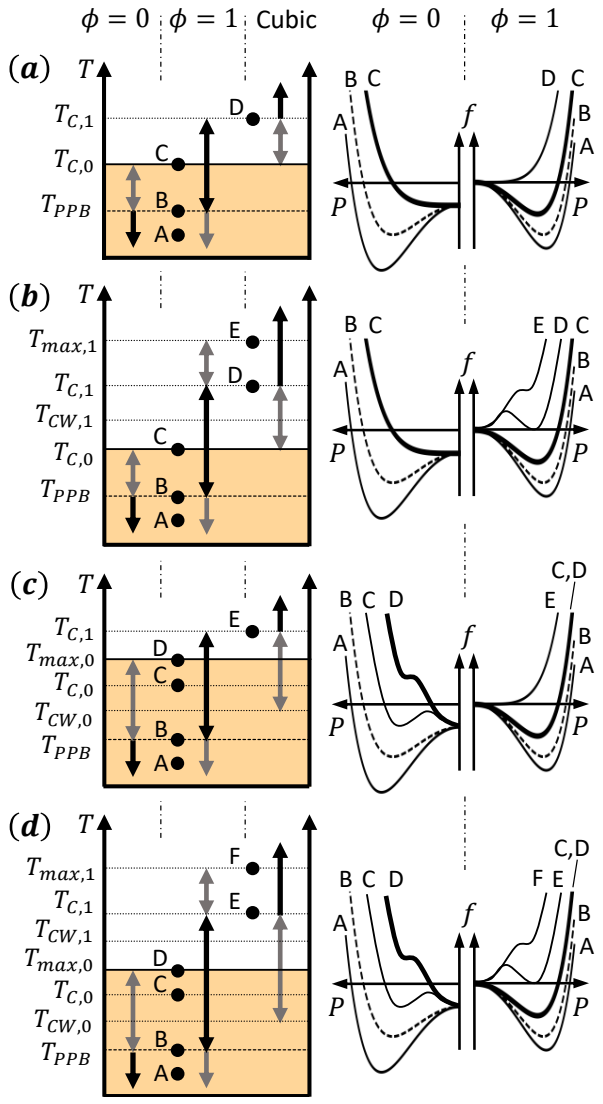

Figure 2: Phase coexistence and stability as a function of P-FE phase transition. Two FE phases are shown: a low-temperature FE phase ($\phi = 0$) and a high-temperature FE phase ($\phi = 1$). Subfigures show (a) second order−second order , (b) second order−first order, (c) first order−second order, and (d) first order−first order interactions. Highlighted area indicates metastable coexistence of the FE phases accessible upon heating or cooling. Free energy curves are sketched on the right for selected temperatures.

Figure 2 predicts a thermal upper limit for the metastable coexistence of the two FE phases. Its extent is a function of the underlying Landau coefficients. When both FE phases display the possibility of a second order P-FE transition, the paraelectric phase is always unstable within the PPB region where the FE phases coexist, Figure 2(a). However, if one of the phases presents a first order P-FE transition, the paraelectric phase will be metastable for temperatures as low as $T = T_{CW}$, Figure 2(b)-(d), giving rise to possi-

ble metastable coexistence of the FE and C phases, which enables polarization switching mechanisms associated with the enhancement of electromechanical properties [3, 18]. For the BZT-xBCT system, coexistence of the R and T ferroelectric phases and the cubic paraelectric phase has been experimentally reported [10].

3. Application to one-dimensional BZT-xBCT

For a system that undergoes polarization switching events along one direction, say $\hat{\imath}$, with an electric field applied along the same direction, we define $\vec{P} = P\hat{\imath}$ and $\vec{E} = E\hat{\imath} = -\partial V_E/\partial x$, where V_E is the electrostatic potential [53]. The polarization switching dynamics are described by two coupled Allen-Cahn equations,

$$\frac{\partial P}{\partial t} = -M_P \left\{ \frac{\partial f_0(P;T)}{\partial P}[1-h(\phi)] + \frac{\partial f_1(P;T)}{\partial P}h(\phi) + \frac{\partial V_E}{\partial x} - K_P \frac{\partial^2 P}{\partial x^2} \right\} \tag{6}$$

$$\frac{\partial \phi}{\partial t} = -M_\phi \left\{ [f_1(P;T) - f_0(P;T)]\frac{\mathrm{d}h(\phi)}{\mathrm{d}\phi} + W\frac{\mathrm{d}g(\phi)}{\mathrm{d}\phi} - K_\phi \frac{\partial^2 \phi}{\partial x^2} \right\} \tag{7}$$

where $K_P = K_{1111}$, $K_\phi = K_{11}$, M_P is the polarization mobility, and M_ϕ is the phase mobility. We set $M_P = M_\phi = M(\phi;T) = M_0(T)[1-h(\phi)] + M_1(T)h(\phi)$, with the mobility of each phase given by $M(T) = M_o \exp(-Q/RT)$.

The electrostatic field distribution is given by Coulomb's Equation in its differential form, $\partial D/\partial x = 0$. The electric displacement is related to the total polarization via the constitutive relation $D = \epsilon_o E + P$, where ϵ_o is the vacuum permittivity [53]. Therefore,

$$-\epsilon_o \frac{\partial^2 V_E}{\partial x^2} + \frac{\partial P}{\partial x} = 0 \tag{8}$$

The model is normalized using $\hat{x} = x/L$, $\hat{t} = t/\tau$, $u = P/|P_{s1}|$, and $\hat{E} = E/|E_{c1}|$, where L is the size of the bulk sample, E_{c1} is the coercive field of the high-temperature phase, and $\tau = 1/(\alpha_{111,1}P_{s1}^4 M_1(T))$. Thus, Equations 6 through 8 are cast in dimensionless form as

$$\frac{1}{\mu}\frac{\partial u}{\partial \hat{t}} = \gamma \hat{\nabla}^2 u - \left\{ \frac{\partial \hat{f}_0(u;T)}{\partial u}[1-h(\phi)] + \frac{\partial \hat{f}_1(u;T)}{\partial u}h(\phi) + \hat{E}_{c1}\frac{\partial \hat{V}_E}{\partial \hat{x}} \right\} \tag{9}$$

$$\frac{1}{\nu}\frac{\partial \phi}{\partial \hat{t}} = \gamma\lambda \hat{\nabla}^2 \phi - \left\{ [\hat{f}_1(u;T) - \hat{f}_0(u;T)]\frac{\partial h(\phi)}{\partial \phi} + \hat{W}\frac{\partial g(\phi)}{\partial \phi} \right\} \tag{10}$$

$$0 = -\hat{\epsilon}_o \frac{\partial^2 \hat{V}_E}{\partial \hat{x}^2} + \frac{\partial u}{\partial \hat{x}} \tag{11}$$

where the following dimensionless parameters are identified: $\mu = M(\phi;T)/M_1(T)$, $\nu = P_{s1}^2\mu$, $\gamma = K_P/(L^2\alpha_{111,1}P_{s1}^4)$, $\lambda = K_\phi/(K_P P_{s1}^2)$, $\hat{W} = W/(\alpha_{111,1}P_{s1}^6)$, $\hat{E}_{c1} = E_{c1}/(\alpha_{111,1}P_{s1}^5)$, and $\hat{\epsilon}_o = \epsilon_o E_{c1}/P_{s1}$.

Further, $\hat{f}_0(u;T)$ and $\hat{f}_1(u;T)$ are given by

$$\hat{f}_1(u;T) = \frac{1}{6}u^6 + \frac{B_1 - 1}{4}u^4 - \frac{B_1}{2}u^2 \tag{12}$$

$$\hat{f}_0(u;T) = \rho\left[\frac{1}{6}u^6 + \frac{B_0 - \eta^2}{4}u^4 - \frac{B_0\eta^2}{2}u^2\right] + \Delta\hat{f}_{PPB} \tag{13}$$

where $B_1 = 1+\alpha_{11,1}/(\alpha_{111,1}P_{s1}^2)$, $B_0 = \eta^2+\alpha_{11,0}/(\alpha_{111,0}P_{s1}^2)$, $\eta = P_{s0}/P_{s1}$, $\rho = \alpha_{111,0}/\alpha_{111,1}$, and $\Delta\hat{f}_{PPB} = \Delta f_{PPB}/(\alpha_{111,1}P_{s1}^6)$. In this model, the order of the P-FE phase transitions depends on the values of B_1, B_0 and η.

Values for the microstructurally averaged Landau coefficients are determined from experimental hysteresis loops for polycrystalline BZT-40BCT ceramics, measured at selected temperatures by Ehmke [49]. While the approach presented herein can be readily extended to estimate the Landau parameters for a single-crystal BZT-40BCT sample, such information was unavailable [54]. The equation $\partial f/\partial P = E = \alpha_1 P+\alpha_{11}P^3+\alpha_{111}P^5$ is fitted to the stable and metastable parts of the hysteresis loops for the unambiguously rhombohedral and tetragonal regions of the phase diagram, see Supplemental Information for details. Mobilities are calculated directly from the BZT-40BCT data at each temperature using $M = 2\pi\omega\chi_c\epsilon_o\sqrt{(E_o/E_c)^2 - 1}$, [55], where $\omega = 0.1\,\mathrm{Hz}$ is the experimental cycling frequency and $E_o = 1\,\mathrm{MV/m}$ is the maximum applied field. Fitted parameters are summarized in Table 1. Mobility values have the same order of magnitude as those reported by Zhao, Cao and García [55] for stress-free, lanthanum-doped PZT.

The PPB temperature is estimated as $T_{PPB} \sim (T_{O-T} + T_{R-O})/2 = 43\,^{\circ}\mathrm{C}$, using $T_{R-O} = 37\,^{\circ}\mathrm{C}$ and $T_{O-T} = 49\,^{\circ}\mathrm{C}$, as reported by Ehmke [49]. The estimated T_{PPB} is approximately equal to the value determined by Liu and Ren [6], Figure 1(b). The dimensionless gradient energy coefficients, $\gamma = 3\times10^{-5}$ and $\lambda = 5.5$, and the double-well coefficient, $\hat{W} = 4$, are established via numerical evaluation such that the widths of the rhombohedral domain wall and the phase interfaces measured in ϕ are approximately equal at $T = T_{PPB}$, the only temperature where both phases are stable. In qualitative agreement with Jona and Shirane [56], the width (ξ) of the rhombohedral domain walls is set to 4 nm, *i.e.,* ten times the characteristic lattice parameter. $L = 190\,\mathrm{nm}$, which is smaller than typical grain sizes of $27 \pm 3\,\mu\mathrm{m}$ for BZT-40BCT [49]. The estimated values for the gradient energy coefficients and the interfacial widths and energies of domain walls, ξ_{DW} and σ_{DW}, and T-R interfaces, ξ_{T-R} and σ_{T-R}, are included in Table 1.

Table 1: Fitted Landau coefficients and mobilities for BZT-40BCT, after experimental data reported by Ehmke [49], and estimated gradient energy coefficients and interfacial widths and energies calculated at $T = T_{PPB} = 43\,^{\circ}\mathrm{C}$.[1]

Symbol	R phase ($\phi = 0$)	T phase ($\phi = 1$)	Units
a_{CW}	5.000×10^4	2.063×10^4	$\mathrm{Jm/C^2K}$
α_{11}	6.314×10^7	-4.229×10^7	$\mathrm{Jm^5/C^4}$
α_{111}	1.263×10^{10}	3.154×10^{10}	$\mathrm{Jm^9/C^6}$
T_{CW}	49.90	69.08	°C
T_C	$T_{CW,0}$	69.60	°C
T_{max}	$T_{CW,0}$	69.77	°C
M_o	1.809×10^{-4}	3.806×10^{-10}	S/m
Q	8561	$-25\,260$	J/mol
K_P	8.922×10^{-13}	8.922×10^{-13}	$\mathrm{Jm^3/C^2}$
K_ϕ	2.383×10^{-14}	2.383×10^{-14}	J/m
σ_{DW}	1.876×10^{-6}	4.063×10^{-6}	$\mathrm{J/m^2}$
σ_{T-R}	4.445×10^{-6}	4.445×10^{-6}	$\mathrm{J/m^2}$
ξ_{DW}	4.000	2.867	nm
ξ_{T-R}	2.834	2.834	nm

For BZT-40BCT, with the Landau coefficients stated in Table 1, the T phase has a weak first order P-FE transition and the R phase has a second order P-FE transition, *i.e.,* the case illustrated in Figure 2(a). The predicted upper limit for metastable coexistence between the R and T phases is $T_{C,0} = 49.9\,^{\circ}\mathrm{C}$, which is approximately equal to $T_{O-T} \sim 49\,^{\circ}\mathrm{C}$, as determined by Ehmke [49], see Figure 1(b). This supports the hypothesis of R+T phase coexistence near the PPB, based on data acquired in the unambiguously single phase regions. Interfacial energies are in agreement with Gao *et al.* [17] and Dam-

[1]Each interfacial energy is calculated via numerical evaluation by $\sigma = \int_0^L [f_{total}(x) - f_{min}]\,dx$ across a computational domain with a single interface, where f_{total} is the total free energy density and f_{min} is the volumetric free energy density corresponding to the stable polarization state(s).

janovic [18].

Figure 3 shows contour plots of the volumetric free energy density of the system at different temperatures and normalized polarization states. In all cases, $u = \pm 1$ is the dimensionless spontaneous polarization of the T phase and $u = \pm\eta$ is the dimensionless spontaneous polarization of the R phase at each temperature. For $\hat{E} = 0$, the global minima in the bulk free energy of the system are located at $u = \pm 1, \phi = 1$, for $T > T_{PPB}$; and at $u = \pm\eta, \phi = 0$, for $T < T_{PPB}$. Results show that direct R↔T transformation between domains with opposing polarization states is inaccessible because of large energy barrier between antiparallel polarization states. Instead, this transformation is achieved by a combination of 180° polarization reversals and R↔T reversible transformations, *i.e.,* polarization rotations, thus defining a mechanism to switching and ferroelectric domain coexistence in the vicinity of the PPB.

For $T < T_{PPB}$, the T phase is metastable, see Figure 3(a). Thus, both T and R phases coexist through formation of domains of opposite polarization and a weak intervening built-in electric field. Energy barriers for polarization switching are different in each phase; for example, at $T = 39\,°\text{C}$ the energy barrier between $u = \pm 1$ in the T phase, $\Delta\hat{f}_1$, is 1.6 times larger than the energy barrier between $u = \pm\eta$ in the R phase, $\Delta\hat{f}_0$. Consequently, switching between rhombohedral domains is possible through two mechanisms, namely: a) via direct 180° polarization reversals; or b) by performing a R→T transformation (rotation), followed by a 180° reversal while in the tetragonal phase, and finally by transforming back to the rhombohedral phase (rotation), *i.e.,* T→R. The second mechanism favours rotation of the polarization order parameter, but requires the thermal energy of the system to be greater than both $\Delta\hat{f}_1$ and the R→T energy of transformation in order to be accessible.

For $T = T_{PPB}$, four thermodynamic equilibrium states are available, see Figure 3(b). The existence of additional polarization directions results in a decrease in polarization anisotropy. At the PPB, the domain switching mechanisms described for the R phase at $T < T_{PPB}$ are possible for both phases, *i.e.,* direct 180° polarization reversal or phase transformations plus 180° reversal (polarization rotation mechanism). As temperature increases, the energy barrier in the R phase decreases such that $\Delta\hat{f}_0 \approx \Delta\hat{f}_1/3$, favouring the formation of rhombohedral domain walls via the direct 180° reversal mechanism. Since $\Delta\hat{f}_1$ and the T→R energy of transformation are equivalent, the likelihood of ob-

serving tetragonal domain walls and T→R transformations is equal. Further, while the polarization rotation mechanism can occur in both phases, the decrease in $\Delta\hat{f}_0$ favours this mechanism in the T phase.

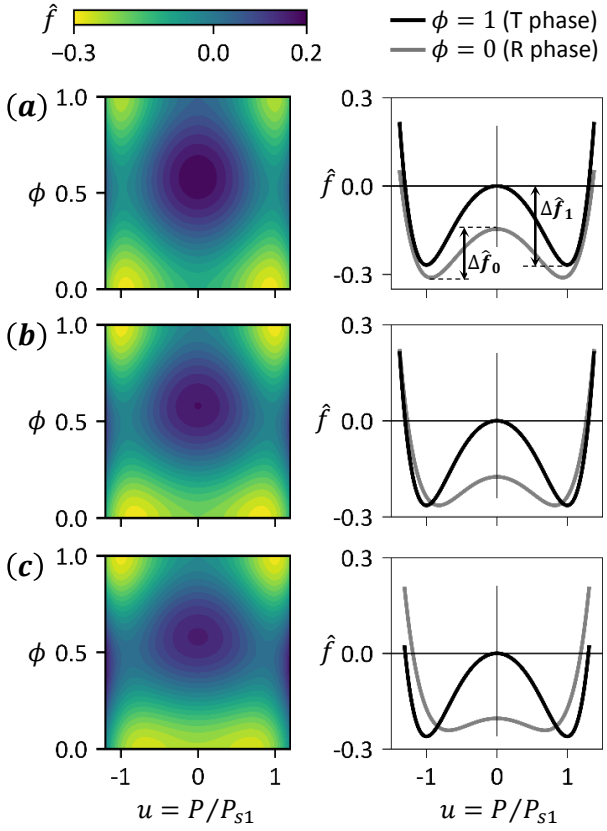

Figure 3: Left column: contour plots of the volumetric free energy density, $\hat{f}(u, \phi; \hat{E} = 0, T) = f/(\alpha_{111,1} P_{s1}^6)$. Right column: volumetic free energy density of R (——) and T (——). Subfigures correspond to (a) $T = 39\,^{\circ}\mathrm{C}$, (b) $T = T_{PPB} = 43\,^{\circ}\mathrm{C}$, and (c) $T = 46\,^{\circ}\mathrm{C}$. In the absence of an applied electric field, both FE phases are equally stable at $T = T_{PPB}$, but metastably persist for a finite range of temperatures away from the PPB line on the phase diagram.

For $T > T_{PPB}$, the R phase becomes metastable, Figure 3(c), and the energy barrier of the R phase further decreases such that $\Delta\hat{f}_0 \approx \Delta\hat{f}_1/7$ at $T = 46\,^{\circ}\mathrm{C}$. Here, the additional thermal energy and the low energy barrier will enable the polarization switching plus rotation mechanism proposed herein, allowing the R phase to persist for very long periods of time.

4. Numerical implementation

The multiphase field model was implemented using FEM in COMSOL Multiphysics® [57]. A 200-element mesh with second-order Lagrange shape functions was used. Simulations took on the order of 25 seconds in an i7-6700 3.4 GHz Quad Core 64 bit processor, with 16 GB of RAM and a Microsoft Windows 7 Enterprise operating system version 6.1.7601.

Hysteretic cycling of BZT-40BCT was simulated at $T = 40.2\,^{\circ}\mathrm{C}$ to validate the model. Equations 9 through 11 were solved with a mixed 50%R+50%T phase initial state. A time-dependent electric field was applied through the boundary conditions $\hat{V}_E(0,\hat{t}) = 0$ and $\hat{V}_E(1,\hat{t}) = \hat{V}_{E,max}\sin(2\pi\hat{\omega}\hat{t})$, where $\hat{V}_{E,max} = -E_o/E_{c1}$ and $\hat{\omega} = \omega\tau$. Zero flux boundary conditions were applied for polarization and for phase field.

The field-free microestructural evolution was simulated at $T = T_{PPB}$ to investigate the phase coexistence of FE phases. Equations 9 and 10 were solved with initial conditions generated from a uniform random distribution, with $\{\mathrm{mean}, \mathrm{range}\}$, for u $\{0, 2\}$ and ϕ $\{0.5, 1\}$. Periodic boundary conditions were applied for both variables (polarization and phase field).

A time-temperature-transformation (TTT) diagram was constructed for the microstructural evolution of the two-phase ferroelectric towards a stable single phase. The fraction transformed of FE phases was measured by ψ, where $\psi = \overline{\phi}$ at $T > T_{PPB}$, and $\psi = 1 - \overline{\phi}$ at $T < T_{PPB}$. Average transformation times for constant fraction transformed were calculated from fifteen computational simulations at selected temperatures. The Johnson-Mehl-Avrami-Kolmogorov (JMAK) equation [58] was fitted to the kinetics of isothermal R+T→T and R+T→R transformations, $\psi = 1 - \exp(-kt^n)$, yielding Avrami exponents $0.29 \leq n \leq 0.55$.

5. Results and discussion

The model was directly compared against polycrystalline experimental data, as reported by Ehmke [49] for $T = 40.2\,^{\circ}\mathrm{C} < T_{PPB}$ and $\omega = 0.1\,\mathrm{Hz}$, Figure 4(a). Very good agreement was found between experiments and the numerical results. Differences near the tails of the hysteresis loops are a result of the slow polarization switching of the last set of domains pinned by grain boundaries, as discussed by Zhao, Bowman and García [59]. Additional comparisons can be found in Figure S2. Further, Figure 4(b) shows that the

application of a cyclic electric field accelerates the R+T→R transformation, measured by the average phase field $\overline{\phi}$, when $\hat{E} \neq 0$.

In a 1D system, the spatial distribution of polarization u is dominated by Coulomb's Equation where $\partial u/\partial \hat{x} \approx 0$. This forces a uniform polarization configuration over the entire system, Figure 4(c)−(e). In 2D and 3D systems, polarization configuration enables access to additional degrees of freedom and will be the subject of future work.

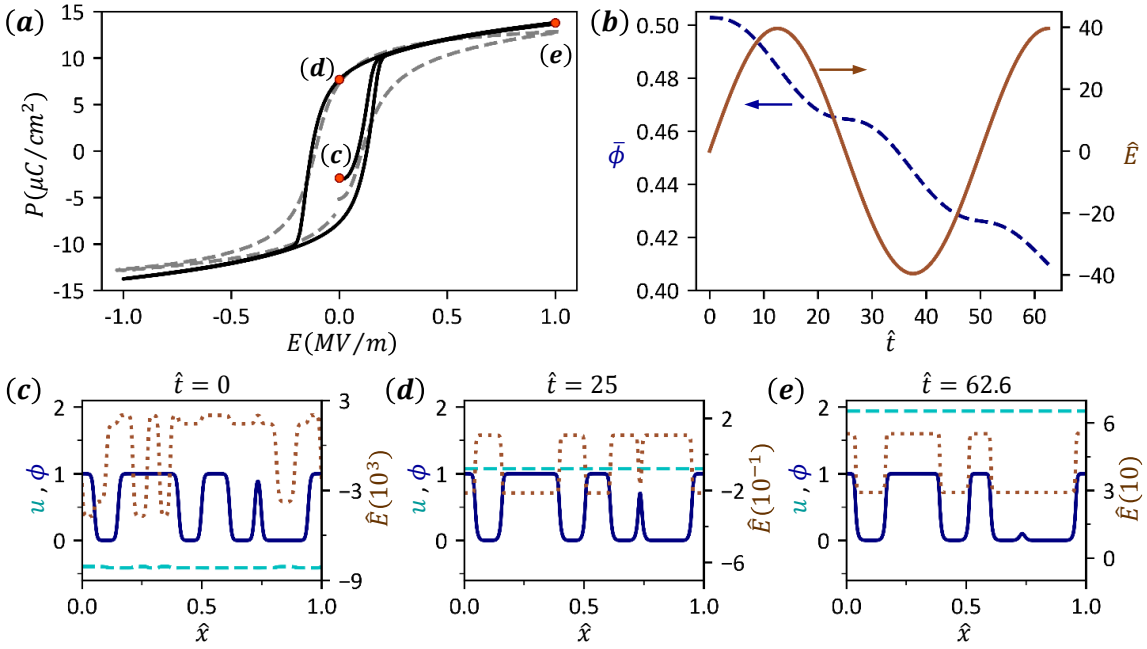

Figure 4: (a) Experimental [49] (- - -) and calculated (——) hysteresis loops at $T = 40.2\,°C$ with $\omega = 0.1\,Hz$ and mixed 50%R+50%T initial condition. (b) Effect of sinusoidal electric field (——) on the average phase field, $\overline{\phi}$ (- - -). Insets (c) through (e) show the spatial distributions of $u = P/P_{s1}$ (- - -, left axis), ϕ (——, left axis), and $\hat{E} = E/E_{c1}$ (·····, right axis) at selected normalized instants $\hat{t} = t/\tau$. Inset (c) shows initial condition ($t = 0$), (d) shows $\hat{t} = 25$ ($t = 5\,s$), and (e) shows $\hat{t} = 62.6$ ($t = 12.5\,s$) after one full cycle.

For $T = T_{PPB}$, Figure 5 shows that rhombohedral and tetragonal domains stably coexist. The average domain size of 20 nm, within the $10 - 60$ nm range as reported by Acosta *et al.* [4], is consistent with miniaturization of the domain structure associated with the decrease in polarization anisotropy [17] and interfacial energy [51] in the vicinity of the PPB. In the absence of an applied electric field, Figure 5 demonstrates that the low energy barrier between variants in the R phase facilitates the formation of rhombohedral domain walls, between states B and C, and enables the polarization rotation as it transitions between states A and D. This is consistent with theoretical results reported by Yang *et*

al. [44] that link the small energy barrier for direct 180° polarization reversal in one phase to the small energy barrier for phase transformation and polarization rotation, identified as the main origin of the enhanced electromechanical properties near the PPB in lead-free materials [43, 60]. Figure 5 also shows that R↔T transformations between domains with opposing polarization states, *e.g.,* between states A and B, occur through a phase transformation, from state A to state C, followed by a 180° polarization reversal, from state C to state B. The presence of local metastable domains, such as those reported herein, have also been simulated by Rao and Wang [42] revealing their role in reducing the total free energy of the system by bridging stable domains.

The formulation developed herein can be readily extended to 2D and includes the effects of mechanical compatibility from the individual ferroelectric variants and interfaces between coexisting phases. This is the subject of future work.

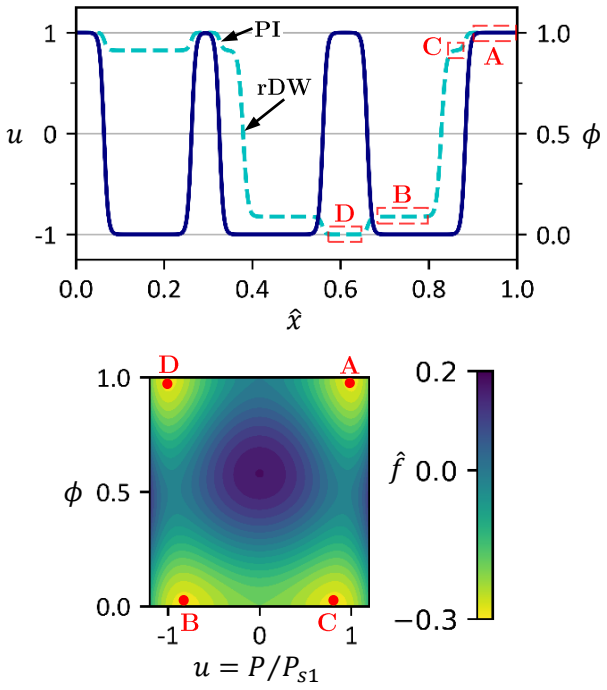

Figure 5: Above: spatial distribution of normalized polarization, $u = P/P_{s1}$ (- - -), and phase field, ϕ (——), at dimensionless time, $\hat{t} = t/\tau = 40000$ at $T = T_{PPB} = 43\,^{\circ}\mathrm{C}$. Below: contour plot of the volumetric free energy density, $\hat{f}(u, \phi; \hat{E} = 0, T) = f/(\alpha_{111,1} P_{s1}^6)$, at $T = T_{PPB} = 43\,^{\circ}\mathrm{C}$. Rhombohedral domain walls (rDW) and phase interfaces (PI) are noted. A, B, C and D represent four equilibrium states. Long term coexistence of R and T phases is observed at the PPB.

Figure 6 shows the macroscopic volume fraction transformed from a mixed 50%R+50%T

state as a function of time at fixed temperature, *i.e.,* a Time-Temperature-Transformation (TTT) diagram. Calculations show that as $T \rightarrow T_{PPB}$ both phases are more likely to coexist. For $T_{PPB} < T < T_{C,0}$, the low-temperature rhombohedral phase coexists metastably with the high-temperature, thermodynamically stable tetragonal phase as a result of the local R↔T phase transformations that are favoured to accommodate local switching events and metastable domains. In contrast, for $T < T_{PPB}$ a decrease in thermal energy suppresses phase transformations and, hence, suppresses the polarization switching plus rotation mechanism. The phase transformation and polarization reversal pathway between domains is possible at all temperatures where the two FE phases can coexist metastably $T < T_{C,0}$. It is favoured at $T > T_{PPB}$ due to the high domain wall energy of the stable phase. Further, the likelihood of observing R+T coexistence decreases with temperature as the driving force for transformation to the most stable phase increases.

The time to reach 55 % transformed volume fraction is one to three orders of magnitude greater for $T > T_{PPB}$ because the available thermal energy enables the polarization switching of the individual phases to accommodate opposing polarization states. This favours the phase transformation-induced polarization rotation mechanism as a means to extend domain coexistence. [2]

[2]The large differences in coexistence time above and below $T = T_{PPB}$, suggest that the true polymorphic phase boundary temperature in the BZT-xBCT system is lower than that suggested by experiments.

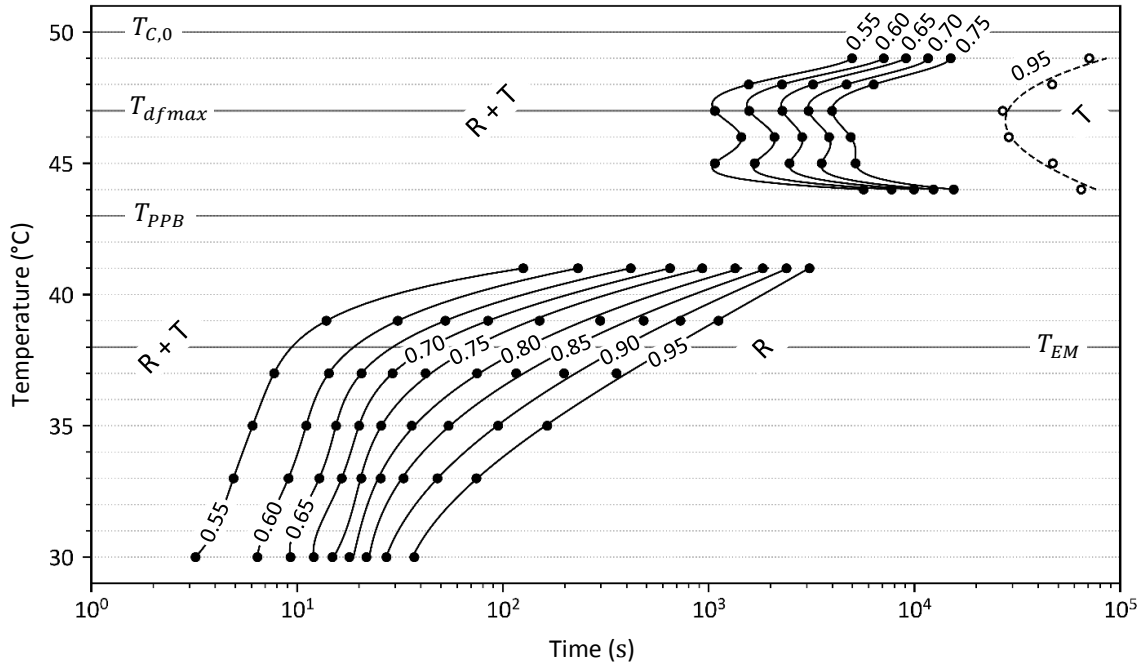

Figure 6: TTT diagram for transformation of mixed R+T phase towards stable single phase as $\psi \to 1$, starting from $\psi = 0.5$ at $t = 0$ at each temperature. Markers represent mean times for constant fraction of phase transformation calculated from 15 computational simulations. Splines are included as a guide for the eye. Estimated times for 0.95 fraction transformed to T phase (- - -) are extrapolated from a JMAK analysis at each $T > T_{PPB}$. T_{dfmax} is the temperature at which the driving force for formation of T phase is maximal, and T_{EM} corresponds to a temperature where mobilities of the FE phases are equal. Metastable coexistence persists for longer times at high temperatures compared to shorter times for R+T→R transformation at lower temperatures.

Macroscopically, for $T < T_{PPB}$, the predicted driving force for transformation to the most stable phase is very large, providing a rationale for the rapid kinetics of phase transformation, Figure 7(a). In addition, the phase-averaged mobility of the system increases with decreasing temperature for $\phi = 0.5$, further promoting fast phase transformation at temperatures less than the PPB, Figure 7(b). For $T_{PPB} > T > T_{EM}$, mobility increases as the transformation progresses and so does the rate of phase transformation; for $T < T_{EM}$, phase transformation kinetics are limited by the mobility of the stable R phase being the lowest of the two phases. For $T > T_{PPB}$, comparatively slow transformation kinetics correspond to a much smaller driving force for R→T transformation, which reaches a maximum at $T = T_{dfmax}$. The rate of phase transformation is again limited

by the low mobility of the stable phase, in this case the T phase, with smaller values of mobility being attained than at $T < T_{PPB}$.

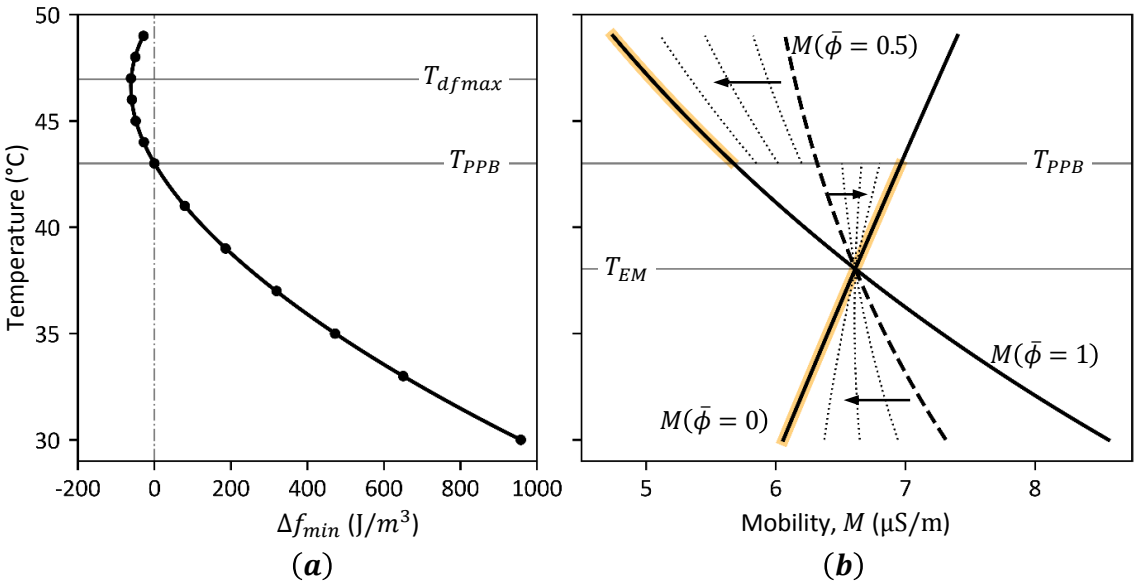

Figure 7: (a) Thermodynamic driving force for transformation of FE phases, $\Delta f_{min} = f_1(P = P_{s1}; E = 0, T) - f_0(P = P_{s0}; E = 0, T)$, and (b) mobility as a function of temperature. There is a local maximum in driving force at T_{dfmax} for the R+T→T transformation. The mobilities of the two phases are equal at T_{EM}. Above T_{PPB} and below T_{EM}, the phase average mobility decreases as $\psi \to 1$, but increases in the range $T_{EM} < T < T_{PPB}$. Metastable coexistence is expected to persist for longer times above T_{PPB} due to smaller driving force and lower mobility.

The coexistence time increases as $T \to T_{C,0}$ for $T_{dfmax} < T < T_{C,0}$. This is attributed to the vanishing R phase domain wall energy, σ^R_{DW}, and the vanishing macroscopic driving force, Δf_{min}, Figure 7(a). The first is a consequence of the second order P-FE transition that occurs for R phase at $T_{C,0}$. The second is a consequence of the fitted Landau coefficients and the selection of a constant Δf_{PPB}.

For $T > T_{C,0}$, the R phase is no longer metastable and any superheated, mixed R+T state is expected to relax to the equilibrium T phase rapidly, in agreement with the phase diagram. No simulations were carried out in this temperature range.

On the one hand, while quantitative results in this study of BZT-40BCT might shift for different gradient energy parameters, the general conclusions would remain the same for this system. On the other hand, if the low temperature phase had a first order P-FE transition, then the domain wall energy would not approach zero as temperature

approached the maximum metastable coexistence temperature, in that case $T = T_{max,0}$. Thus the coexistence time would be unlikely to increase for $T \to T_{max,0}$, as predicted for BZT-40BCT. This predicted behaviour must be explored for material chemistries exhibiting an interferroelectric transition and appropriate FE phase behaviours.

6. Summary and conclusions

A phase field theory for ferroelectric systems in the vicinity of the polymorphic phase boundary is proposed. Based on a multiphase field formulation, the model considers the thermodynamics of individual phases independently, in order to assess equilibrium states and phase transformation dynamics of two competing ferroelectric phases. The model was applied to the BZT-40BCT system and identifies conditions for the stable and metastable coexistence of the rhombohedral and tetragonal phases, as well as an upper limit for metastability, $T_{C,0} = 49.9\,^{\circ}\mathrm{C}$. While there is no thermodynamic limit on metastability for $T < T_{PPB}$, results demonstrate that coexistence is short lived (on the order of tens of seconds), whereas coexistence persists from minutes to hours for $T > T_{PPB}$. Further, metastable coexistence of phases provides access to additional polarization directions, which enables a phase transformation-induced polarization rotation mechanism near the interferroelectric phase boundary. The proposed polarization rotation mechanism is a local intervening kinetic step that is partially responsible for the enhancement of ferroelectric properties.

7. Acknowledgements

This work was supported by the University of Canterbury (College of Engineering PhD Scholarship). REG thanks the Erskine Fellowship, and the partial support from NSF grant 1734763. The authors thank M. C. Ehmke and J. E. Blendell for sharing their experimental data.

References

[1] A. J. Bell, Ferroelectrics: The role of ceramic science and engineering, JECS 28 (7) (2008) 1307–1317. doi:10.1016/j.jeurceramsoc.2007.12.014.

[2] J. Rödel, W. Jo, K. T. P. Seifert, E.-M. Anton, T. Granzow, D. Damjanovic, Perspective on the development of lead-free piezoceramics, JACerS 92 (6) (2009) 1153–1177. doi:10.1111/j.1551-2916.2009.03061.x.

[3] D. Damjanovic, N. Klein, J. Li, V. Porokhonskyy, What can be expected from lead-free piezoelectric materials?, FML 3 (1) (2010) 5–13. doi:10.1142/S1793604710000919.

[4] M. Acosta, N. Novak, V. Rojas, S. Patel, R. Vaish, J. Koruza, G. A. Rossetti, J. Rödel, $BaTiO_3$-based piezoelectrics: Fundamentals, current status, and perspectives, 04 4 (4) (2017) 041305. doi:10.1063/1.4990046.

[5] J. Gao, D. Xue, W. Liu, C. Zhou, X. Ren, Recent progress on $BaTiO_3$-based piezoelectric ceramics for actuator applications, Actuators 6 (3) (2017) 24. doi:10.3390/act6030024.

[6] W. Liu, X. Ren, Large piezoelectric effect in Pb-free ceramics, PRL 103 (25) (2009) 257602. doi:10.1103/PhysRevLett.103.257602.

[7] D. S. Keeble, F. Benabdallah, P. A. Thomas, M. Maglione, J. Kreisel, Revised structural phase diagram of $(Ba_{0.7}Ca_{0.3}TiO_3)$-$(BaZr_{0.2}Ti_{0.8}O_3)$, APL 102 (9) (2013) 092903. doi:10.1063/1.4793400.

[8] L. Zhang, M. Zhang, L. Wang, C. Zhou, Z. Zhang, Y. G. Yao, L. X. Zhang, D. Z. Xue, X. J. Lou, X. B. Ren, Phase transitions and the piezoelectricity around morphotropic phase boundary in $Ba(Zr_{0.2}Ti_{0.8})O_3$-x$(Ba_{0.7}Ca_{0.3})TiO_3$ lead-free solid solution, APL 105 (16) (2014) 162908. doi:10.1063/1.4899125.

[9] D. Damjanovic, A. Biancoli, L. Batooli, A. Vahabzadeh, J. Trodahl, Elastic, dielectric, and piezoelectric anomalies and Raman spectroscopy of $0.5Ba(Ti_{0.8}Zr_{0.2})O_3$-$0.5(Ba_{0.7}Ca_{0.3})TiO_3$, APL 100 (19) (2012) 192907. doi:10.1063/1.4714703.

[10] M. C. Ehmke, S. N. Ehrlich, J. E. Blendell, K. J. Bowman, Phase coexistence and ferroelastic texture in high strain (1-x)$Ba(Zr_{0.2}Ti_{0.8})O_3$-x$(Ba_{0.7}Ca_{0.3})TiO_3$ piezoceramics, JAP 111 (12) (2012) 124110. doi:10.1063/1.4730342.

[11] G. Singh, V. Sathe, V. S. Tiwari, Investigation of rhombohedral-to-tetragonal phase transition in $0.5Ba(Ti_{0.8}Zr_{0.2})$-$0.5(Ba_{0.7}Ca_{0.3})TiO_3$ lead-free ferroelectric using micro-Raman scattering, JEM 46 (8) (2017) 4976–4980. doi:10.1007/s11664-017-5512-y.

[12] J. H. Gao, L. X. Zhang, D. Z. Xue, T. Kimoto, M. H. Song, L. S. Zhong, X. B. Ren, Symmetry determination on Pb-free piezoceramic $0.5Ba(Zr_{0.2}Ti_{0.8})O_3$-$0.5(Ba_{0.7}Ca_{0.3})TiO_3$ using convergent beam electron diffraction method, JAP 115 (5) (2014) 054108. doi:10.1063/1.4864130.

[13] A. B. Haugen, J. S. Forrester, D. Damjanovic, B. Z. Li, K. J. Bowman, J. L. Jones, Structure and phase transitions in $0.5(Ba_{0.7}Ca_{0.3}TiO_3)$-$0.5(BaZr_{0.2}Ti_{0.8}O_3)$ from -100 °C to 150 °C, JAP 113 (1) (2013) 014103. doi:10.1063/1.4772741.

[14] A. A. Heitmann, G. A. Rossetti, Thermodynamics of ferroelectric solid solutions with morphotropic phase boundaries, JACerS 97 (6) (2014) 1661–1685. doi:10.1111/jace.12979.

[15] G. A. Rossetti Jr, A. G. Khachaturyan, G. Akcay, Y. Ni, Ferroelectric solid solutions with morphotropic boundaries: Vanishing polarization anisotropy, adaptive, polar glass, and two-phase states, JAP 103 (11) (2008) 114113. doi:10.1063/1.2930883.

[16] M. Acosta, N. Khakpash, T. Someya, N. Novak, W. Jo, H. Nagata, G. A. Rossetti, J. Rödel, Origin of the large piezoelectric activity in (1-x)$Ba(Zr_{0.2}Ti_{0.8})O_3$-x$(Ba_{0.7}Ca_{0.3})TiO_3$ ceramics, PRB 91 (10) (2015) 104108. doi:10.1103/PhysRevB.91.104108.

[17] J. H. Gao, X. H. Hu, Y. B. Liu, Y. Wang, X. Q. Ke, D. Wang, L. S. Zhong, X. B. Ren, Ferroelectric domain walls approaching morphotropic phase boundary, JPCC 121 (4) (2017) 2243–2250. doi:10.1021/acs.jpcc.6b11595.

[18] D. Damjanovic, A morphotropic phase boundary system based on polarization rotation and polarization extension, APL 97 (6) (2010) 062906. doi:10.1063/1.3479479.

[19] R. Cohen, Theory of ferroelectrics: A vision for the next decade and beyond, JPCS 61 (2) (2000) 139–146. doi:10.1016/S0022-3697(99)00272-3.

[20] B. Völker, P. Marton, C. Elsässer, M. Kamlah, Multiscale modeling for ferroelectric materials: A transition from the atomic level to phase-field modeling, CMT 23 (5) (2011) 435–451. doi:10.1007/s00161-011-0188-7.

[21] B. Meyer, D. Vanderbilt, *Ab Initio* study of ferroelectric domain walls in $PbTiO_3$, PRB 65 (10) (2002) 104111. doi:10.1103/PhysRevB.65.104111.

[22] G. Pilania, R. Ramprasad, Complex polarization ordering in $PbTiO_3$ nanowires: A first-principles computational study, PRB 82 (15) (2010) 155442. doi:10.1103/PhysRevB.82.155442.

[23] T. Shimada, S. Tomoda, T. Kitamura, *Ab Initio* study of ferroelectric closure domains in ultrathin $PbTiO_3$ films, PRB 81 (14) (2010) 144116. doi:10.1103/PhysRevB.81.144116.

[24] A. Grünebohm, M. E. Gruner, P. Entel, Domain structure in the tetragonal phase of $BaTiO_3$ - from bulk to nanoparticles, Ferroelectrics 426 (1) (2012) 21–30. doi:10.1080/00150193.2012.671090.

[25] V. Boddu, F. Endres, P. Steinmann, Molecular dynamics study of ferroelectric domain nucleation and domain switching dynamics, SR 7 (1) (2017) 806. doi:10.1038/s41598-017-01002-0.

[26] M. Sepliarsky, A. Asthagiri, S. Phillpot, M. Stachiotti, R. Migoni, Atomic-level simulation of ferroelectricity in oxide materials, COSSMS 9 (3) (2005) 107–113. doi:10.1016/j.cossms.2006.05.002.

[27] J. Paul, T. Nishimatsu, Y. Kawazoe, U. V. Waghmare, Polarization rotation, switching, and electric-field–temperature phase diagrams of ferroelectric $BaTiO_3$: A molecular dynamics study, PRB 80 (2) (2009) 024107. doi:10.1103/PhysRevB.80.024107.

[28] Y. Sang, B. Liu, D. Fang, The size and strain effects on the electric-field-induced domain evolution and hysteresis loop in ferroelectric $BaTiO_3$ nanofilms, CMS 44 (2) (2008) 404–410. doi:10.1016/j.commatsci.2008.04.001.

[29] T. Shimada, K. Wakahara, Y. Umeno, T. Kitamura, Shell model potential for $PbTiO_3$ and its applicability to surfaces and domain walls, JPCM 20 (32) (2008) 325225. doi:10.1088/0953-8984/20/32/325225.

[30] Y. Zhang, R. Xu, B. Liu, D. Fang, An electromechanical atomic-scale finite element method for simulating evolutions of ferroelectric nanodomains, JMPS 60 (8) (2012) 1383–1399. doi:10.1016/j.jmps.2012.04.012.

[31] P. Marton, I. Rychetsky, J. Hlinka, Domain walls of ferroelectric $BaTiO_3$ within the Ginzburg-Landau-Devonshire phenomenological model, PRB 81 (14) (2010) 144125. doi:10.1103/PhysRevB.81.144125.

[32] W. Zhang, K. Bhattacharya, A computational model of ferroelectric domains. Part I: Model formulation and domain switching, AM 53 (1) (2005) 185—198. doi:10.1016/j.actamat.2004.09.016.

[33] J. Wang, S.-Q. Shi, L.-Q. Chen, Y. Li, T.-Y. Zhang, Phase-field simulations of ferroelectric/ferroelastic polarization switching, AM 52 (3) (2004) 749–764. doi:10.1016/j.actamat.2003.10.011.

[34] Y. C. Song, Y. Ni, J. Q. Zhang, Phase field model of polarization evolution in a finite ferroelectric body with free surfaces, AMech 224 (6) (2013) 1309–1313. doi:10.1007/s00707-013-0858-6.

[35] H.-L. Hu, L.-Q. Chen, Three-dimensional computer simulation of ferroelectric domain formation, JACerS 81 (1998) 492–500.

[36] T. Koyama, H. Onodera, Phase-field simulation of ferroelectric domain microstructure changes in $BaTiO_3$, MT 50 (5) (2009) 970–976. doi:10.2320/matertrans.MC200806.

[37] W. D. Dong, D. M. Pisani, C. S. Lynch, A finite element based phase field model for ferroelectric domain evolution, SMS 21 (9) (2012) 094014. doi:10.1088/0964-1726/21/9/094014.

[38] W. Zhang, K. Bhattacharya, A computational model of ferroelectric domains. Part II: Grain boundaries and defect pinning, AM 53 (1) (2005) 199–209. doi:10.1016/j.actamat.2004.09.015.

[39] S. Choudhury, Y. L. Li, C. E. Krill, L.-Q. Chen, Phase-field simulation of polarization switching and domain evolution in ferroelectric polycrystals, AM 53 (20) (2005) 5313–5321. doi:10.1016/j.actamat.2005.07.040.

[40] L.-Q. Chen, Phase-field method of phase transitions/domain structures in ferroelectric thin films: A review, JACerS 91 (6) (2008) 1835–1844. doi:10.1111/j.1551-2916.2008.02413.x.

[41] X. L. Wang, B. Li, X. L. Zhong, Y. Zhang, J. B. Wang, Y. C. Zhou, Effects of space charge distribution on ferroelectric hysteresis loops considering the inhomogeneous built-in electric field: A phase field simulation, JAP 112 (11) (2012) 114103. doi:10.1063/1.4767702.

[42] W.-F. Rao, Y. U. Wang, Bridging domain mechanism for phase coexistence in morphotropic phase boundary ferroelectrics, APL 90 (18) (2007) 182906. doi:10.1063/1.2736276.

[43] X. Q. Ke, D. Wang, Y. Wang, Origin of ultrahigh piezoelectric activity of [001]-oriented ferroelectric single crystals at the morphotropic phase boundary, APL 108 (1) (2016) 012904. doi:10.1063/1.4939626.

[44] T. Yang, X. Ke, Y. Wang, Mechanisms responsible for the large piezoelectricity at the tetragonal-orthorhombic phase boundary of (1-x)$BaZr_{0.2}Ti_{0.8}O_3$-x$Ba_{0.7}Ca_{0.3}TiO_3$ system, SR 6 (2016) 33392. doi:10.1038/srep33392.

[45] L. Liang, Y. L. Li, L.-Q. Chen, S. Y. Hu, G.-H. Lu, Thermodynamics and ferroelectric properties of $KNbO_3$, JAP 106 (10) (2009) 104118. doi:10.1063/1.3260242.

[46] Z. Ma, L. Xi, H. Liu, F. Zheng, H. Gao, Z. Chen, H. Chen, Ferroelectric phase transition of $BaTiO_3$ single crystal based on a tenth order Landau-Devonshire potential, CMS 135 (2017) 109–118. doi:10.1016/j.commatsci.2017.04.011.

[47] Y. L. Wang, A. K. Tagantsev, D. Damjanovic, N. Setter, V. K. Yarmarkin, A. I. Sokolov, I. A. Lukyanchuk, Landau thermodynamic potential for $BaTiO_3$, JAP 101 (10) (2007) 104115. doi:10.1063/1.2733744.

[48] F. Xue, Y. Ji, L.-Q. Chen, Theory of strain phase separation and strain spinodal: Applications to ferroelastic and ferroelectric systems, AM 133 (2017) 147–159. doi:10.1016/j.actamat.2017.05.028.

[49] M. C. Ehmke, Ferroelastic domains in lead-free barium zirconate titanate - barium calcium titanate piezoceramics, Ph.D. thesis, ProQuest, UMI Dissertations Publishing (2014).

[50] J. A. Warren, W. J. Boettinger, Prediction of dendritic growth and microsegregation patterns in a binary alloy using the phase-field method, AMM 43 (2) (1995) 689–703. doi:10.1016/0956-7151(94)00285-P.

[51] M. E. Lines, A. M. Glass, Principles and Applications of Ferroelectrics and Related Materials, Oxford University Press, Oxford, 2001.

[52] K. S. N. Vikrant, W. C. Chueh, R. E. Garćia, Charged interfaces: Electrochemical and mechanical effects, EES (2018) .doi:10.1039/C7EE03400H.

[53] J. D. Jackson, Classical Electrodynamics, 3rd Edition, Wiley, New York, 1999.

[54] J. Hou, Y. Wu, Z. Wang, Analytical intrinsic electromechanical properties of ferroelectric ceramics under the saturated and unsaturated poling states, Computational Materials Science 96 (2015) 327–335. doi:10.1016/j.commatsci.2014.08.046.

[55] Z. Zhao, Y. Cao, R. E. Garćia, Kinetically stabilized metastable polarization states in ferroelectric ceramics, JECS 37 (2) (2017) 573–581. doi:10.1016/j.jeurceramsoc.2016.08.022.

[56] F. Jona, G. Shirane, Ferroelectric Crystals, Vol. 1 of International series of monographs on solid state physics, The Macmillan Company, New York, 1962.

[57] COMSOL Multiphysics® v. 5.2. www.comsol.com. COMSOL AB, Stockholm, Sweden.

[58] R. E. Reed-Hill, R. Abbaschian, Physical Metallurgy Principles, 3rd Edition, The PWS-Kent series in engineering, PWS-Kent Pub, Boston, 1992.

[59] Z. Zhao, K. Bowman, R. E. Garćia, Modeling 180 domain switching population dynamics in polycrystalline ferroelectrics, Journal of the American Ceramic Society 95 (5) (2012) 1619–1627. doi:10.1111/j.1551-2916.2011.05023.x.

[60] F. Rubio-Marcos, R. López-Juárez, R. E. Rojas-Hernandez, A. del Campo, N. Razo-Pérez, J. F. Fernandez, Lead-free piezoceramics: Revealing the role of the rhombohedral-tetragonal phase coexistence in enhancement of the piezoelectric properties, ACS 7 (41) (2015) 23080–23088. doi:10.1021/acsami.5b06747.